Earth and Planetary Science Letters 429 (2015) 223–233

Contents lists available at ScienceDirect

Earth and Planetary Science Letters

www.elsevier.com/locate/epsl

Timescales for permeability reduction and strength recovery in densifying magma

M.J. Heap[a,*], J.I. Farquharson[a], F.B. Wadsworth[b], S. Kolzenburg[c], J.K. Russell[d]

[a] Géophysique Expérimentale, Institut de Physique de Globe de Strasbourg (UMR 7516 CNRS, Université de Strasbourg/EOST), 5 rue René Descartes, 67084 Strasbourg cedex, France

[b] Department for Earth and Environmental Sciences, Ludwig-Maximilians-Universität, Munich, Theresienstr. 41/III, 80333 Munich, Germany

[c] Dipartimento di Scienze della Terra, Università degli Studi di Torino, 35 Via Valperga Caluso, 10125, Torino, Italy

[d] Volcanology and Petrology Laboratory, Department of Earth and Ocean Sciences, University of British Columbia, Vancouver, V6T 1Z4, Canada

ARTICLE INFO

Article history:
Received 6 April 2015
Received in revised form 21 July 2015
Accepted 24 July 2015
Available online 18 August 2015
Editor: T.A. Mather

Keywords:
welding
changepoint
P-wave velocity
uniaxial compressive strength
fracture healing
outgassing

ABSTRACT

Transitions between effusive and explosive behaviour are routine for many active volcanoes. The permeability of the system, thought to help regulate eruption style, is likely therefore in a state of constant change. Viscous densification of conduit magma during effusive periods, resulting in physical and textural property modifications, may reduce permeability to that preparatory for an explosive eruption. We present here a study designed to estimate timescales of permeability reduction and strength recovery during viscous magma densification by coupling measurements of permeability and strength (using samples from a suite of variably welded, yet compositionally identical, volcanic deposits) with a rheological model for viscous compaction and a micromechanical model, respectively. Bayesian Information Criterion analysis confirms that our porosity–permeability data are best described by two power laws that intersect at a porosity of 0.155 (the "changepoint" porosity). Above and below this changepoint, the permeability–porosity relationship has a power law exponent of 8.8 and 1.0, respectively. Quantitative pore size analysis and micromechanical modelling highlight that the high exponent above the changepoint is due to the closure of wide (∼200–300 μm) inter-granular flow channels during viscous densification and that, below the changepoint, the fluid pathway is restricted to narrow (∼50 μm) channels. The large number of such narrow channels allows porosity loss without considerable permeability reduction, explaining the switch to a lower exponent. Using these data, our modelling predicts a permeability reduction of four orders of magnitude (for volcanically relevant temperatures and depths) and a strength increase of a factor of six on the order of days to weeks. This discrepancy suggests that, while the viscous densification of conduit magma will inhibit outgassing efficiency over time, the regions of the conduit prone to fracturing, such as the margins, will likely persistently re-fracture and keep the conduit margin permeable. The modelling therefore supports the notion that repeated fracture-healing cycles are responsible for the successive low-magnitude earthquakes associated with silicic dome extrusion. Taken together, our results indicate that the transition from effusive to explosive behaviour may rest on the competition between permeability reduction within the conduit and outgassing through fractures at the conduit margin. If the conditions for explosive behaviour are satisfied, the magma densification clock will be reset and the process will start again. The timescales of permeability reduction and strength recovery presented in this study may aid our understanding of the permeability evolution of conduit margin fractures, magma fracture-healing cycles, surface outgassing cycles, and the timescales required for pore pressure augmentation and the initiation of explosive eruptions.

1. Introduction

Welding of volcanic materials occurs through the viscous sintering, compaction, and agglutination of melt particles above their glass transition temperature (e.g., Grunder and Russell, 2005). Welding can occur in the absence of an external load through surface relaxation (Vasseur et al., 2013), but can be assisted by the additional stress provided by the mass of any overlying material (e.g., Quane et al., 2009) or by shear strain (e.g., Tuffen et al., 2003; Kolzenburg and Russell, 2014). The prevalence of welding examples in volcanic environments highlights the importance for thor-

* Corresponding author.
E-mail address: heap@unistra.fr (M.J. Heap).

http://dx.doi.org/10.1016/j.epsl.2015.07.053
0012-821X/

ough investigation of the influence of viscous densification on magma physical properties. For example, evidence for welding has been observed in pyroclastic deposits (e.g., Wright and Cashman, 2013) including block-and-ash flow deposits (e.g., Michol et al., 2008; Andrews et al., 2014; Heap et al., 2014a), lava spatter (e.g., Mellors and Sparks, 1991), autobreccias in blocky-lavas and dome lavas (e.g., Sparks et al., 1993), autobreccias at the base of rheomorphic ignimbrites (e.g., Branney et al., 1992), conduit-filling pyroclastic deposits (e.g., Kano et al., 1997; Kolzenburg and Russell, 2014), and rhyolitic dykes and conduits (e.g., Tuffen et al., 2003; Tuffen and Dingwell, 2005; Okumura and Sasaki, 2014). Welding results in densification, modifying the physical and textural properties of the material. Indeed, welding has been shown to increase the density and strength and decrease the porosity and permeability of volcanic materials and analogues (e.g., Quane et al., 2009; Vasseur et al., 2013; Wright and Cashman, 2013; Okumura and Sasaki, 2014; Heap et al., 2014a). Ultimately, the evolution of physical properties can govern the timescales and extent of welding, the potential for rheomorphic flow, and volcanic explosivity. For example, the ease with which magma can outgas, controlled by the permeability of the system, can influence eruption style, magnitude, and frequency (e.g., Eichelberger et al., 1986; Woods and Koyaguchi, 1994). While the majority of laboratory studies considering the relationships between porosity and permeability for volcanic rocks have focussed on the consequence of ascent-driven vesiculation and bubble growth (porosity increase) for magma permeability (e.g., Eichelberger et al., 1986; Klug and Cashman, 1996; Saar and Manga, 1999; Blower, 2001; Rust and Cashman, 2004; Heap et al., 2014b; Farquharson et al., 2015, amongst others), there are comparatively few laboratory investigations that consider the impact of porosity destruction through magma densification (e.g., Wright and Cashman, 2013; Kendrick et al., 2013; Okumura and Sasaki, 2014; Heap et al., 2014a). Between individual explosive events, porous magma residing in a conduit spends a significant portion of time deforming under the mass of the overlying magmatic column at temperatures above the glass transition of the melt phase. During these intervals, a reduction in the magma permeability through viscous densification could lead to the build-up of pore pressure required for the development of an explosive eruption (e.g., Melnik et al., 2005; Diller et al., 2006). Here we report on a coupled experimental and modelling study that aims to better understand the timescales required to reduce permeability and increase strength during viscous magma densification.

2. Materials and methods

2.1. Materials and sample preparation

This study utilises a suite of natural blocks (about 30 × 30 × 30 cm) collected from the variably-welded block-and-ash flow (BAF) deposits that formed following the 2360 B.P. eruption of Mount Meager volcano (part of the Garibaldi Volcanic Belt, the northernmost segment of the Cascade Volcanic Arc of North America; see Michol et al., 2008; Andrews et al., 2014). The BAF deposits—initially >160 m thick—filled and dammed the Lillooet River valley. The densely-welded portions of the deposit are currently exposed in a 100 m rock wall that formed following the collapse of the pyroclastic dam and erosion from the concomitant flood. The clast sizes in the deposits are typically 5–15 cm in diameter, with rare large clasts up to 1 m. The matrix comprises vitric and crystal fragments (and occasional lithics) that are generally less than 1–2 mm in diameter (see Michol et al., 2008 and Andrews et al., 2014 for a full description of the deposit). The welding intensity of these compositionally similar BAF deposits (Stewart, 2002) ranges from incipient (>0.2 porosity) to dense (<0.1 porosity) (Michol et al., 2008; Heap et al., 2014a) and therefore provides the perfect opportunity to study the influence of viscous densification on material physical properties. Typical welding microtextures (e.g., clast elongation/flattening) found within the deposit are described in detail in Michol et al. (2008) and Heap et al. (2014a) (but also provided here as Figs. 3b and 3c). Using field texture maps, Michol et al. (2008) measured the average volumetric and pure shear strain recorded in these BAF deposits to be 42% (highest 92%) and 31% (highest 82%), respectively. We also sampled a fresh (non-oxidised), glassy block from the incipiently welded facies; we anticipate that this material best represents the source material for the BAF deposit. We analysed optical microscope photomicrographs of a sample of this lava using image processing software ImageJ to estimate the average crystal content of our welded materials. We estimated crystal content to be 0.25 (phenocrysts and minor microlites), the remainder of the sample comprising porosity (0.04–0.05) and a glassy groundmass (Fig. 3a). The dominant crystal size within the source material is between 100 and 400 μm, although we note the presence of occasional phenocrysts as large as a couple of mm and minor microlites (<100 μm) (Fig. 3a).

Table 1
Whole rock geochemistry (determined by X-ray fluorescence) and glass geochemistry (determined using an electron microprobe) for the materials of this study (data from Stewart, 2002).

Oxide	Whole rock (wt.%)	Glass (wt.%)
SiO_2	67.51	76.41
TiO_2	0.47	0.30
Al_2O_3	15.78	13.11
Fe_2O_3	3.40	1.20
MgO	1.48	0.26
CaO	3.44	1.18
Na_2O	4.60	4.41
K_2O	2.51	3.52
P_2O_5	0.16	–
LOI	0.70	–
Total	100.06	99.38

We prepared cylindrical samples, 20 mm in diameter and precision-ground to nominal lengths of 40 mm, from the blocks collected (the welded blocks and the lava block). Due to the size of our experimental samples, cores from the welded blocks were prepared so as to avoid any large (5–15 cm) clasts. Our welded BAF samples therefore contain vitric and crystal fragments (and occasional lithics) that are generally less than 1–2 mm in diameter (as shown in Figs. 3b and 3c; Michol et al., 2008). We further note that, in general, vitric fragments are larger than the crystal fragments (a consequence of the dominant crystal size, 100–400 μm, in the source material). The cores were then vacuum-dried at 40 °C for at least two days prior to measurement and experimentation.

The bulk composition of our materials is dacitic (SiO_2 = 68 wt.%) with a rhyolitic glass groundmass (SiO_2 = 76 wt.%); the wt.% of major oxides for both the bulk material and the glass are provided in Table 1 (data from Stewart, 2002).

2.2. Methods

Porosity and permeability were measured for each of the prepared cylindrical cores at the Université de Strasbourg (France). Connected porosity was measured using a helium pycnometer (for brevity, connected porosity will be simply referred to as "porosity" in the remainder of this manuscript). Steady-state gas (nitrogen) permeability was measured under a confining pressure of 1 MPa. Flow rate measurements were taken (using a gas flowmeter) under several pressure gradients (typically from 0.05 to 0.2 MPa) to determine the permeability using Darcy's law, and to assess the need for the Klinkenberg or Forchheimer correction. Klinkenberg corrections were applied where appropriate, but our flow rates were never high enough to warrant a Forchheimer correction in these materials. Physical property data of five additional samples (25.4 mm in diameter and nominally 50 mm in length) were measured at the University of British Columbia (Canada). Porosity was again determined using helium pycnometry, while permeability (helium) was measured using the pulse decay technique under confining pressures between 2.5 and 15 MPa, corresponding to depths up to 1000 m (estimated using $\sigma = \rho g h$, where ρ is taken as the skeletal density of the lava sample—measured to be 2500 $kg\,m^{-3}$ using helium pycnometry—multiplied by 0.6, and g as 10 $m\,s^{-2}$). To aid our understanding of the progression of microstructural modification during viscous densification, we performed complementary P-wave velocity measurements. P-wave velocity was measured along the axis of the samples under a constant axial stress of 0.3 MPa. Finally, uniaxial compressive strength was measured using a uniaxial compression apparatus under a constant strain rate of 10^{-5} s^{-1}. A displacement transducer (LVDT) monitored the axial shortening of the sample by recording the movement of the axial piston relative to the static baseplate. Measurements of axial shortening were corrected for the elastic deformation of the loading train. A load cell monitored the axial force. Displacement and load were converted to strain and stress using the sample dimensions. The broken samples were then powdered, the density of which (the skeletal density) was used to calculate total porosity. Isolated porosity was simply taken as total porosity minus connected porosity. All physical property measurements were performed under ambient laboratory pressure (with the exception of the permeability measurements), temperature, and humidity.

3. Results

Measured values of permeability, P-wave velocity, and uniaxial compressive strength are plotted as a function of porosity in Fig. 1. A summary of the physical property characterisation is provided in Tables 2, 3, and 4. The data show that, as porosity decreases, permeability decreases (Fig. 1a), and P-wave velocity (Fig. 1b) and strength (Fig. 1c) increase. The highest permeabilities, $\sim 10^{-13}$ m^2, were measured for the most porous welded BAF samples (porosity = 0.25); at the lowest porosity—the lava samples with a porosity of 0.04—values of permeability are about two orders of magnitude lower ($\sim 10^{-15}$ m^2). The decrease in permeability with decreasing porosity is nonlinear. In detail, the permeability decrease with decreasing porosity is large between a porosity of 0.25 to 0.15–0.16, and markedly smaller between porosities of 0.16 and 0.04 (Fig. 1a). By contrast, the increase in P-wave velocity (Fig. 1b) and strength (Fig. 1c) with decreasing porosity are very nearly linear, although a break in slope in the strength data may exist at 0.15–0.16 porosity. P-wave velocity increases from $\sim$2.0 $km\,s^{-1}$ at 0.25 porosity to $\sim$3.0 $km\,s^{-1}$ at a porosity of 0.04. The strength at 0.25 porosity is $\sim$15 MPa, which increases to $\sim$85 MPa at a porosity of 0.07.

The influence of confining pressure (up to 15 MPa, corresponding to a maximum depth of 1000 m) on the permeability of two welded BAF samples (with initial porosities of 0.172 and 0.195, respectively) and a sample of lava (porosity = 0.047) is presented in Fig. 2. We find that the permeability of the welded BAF samples does not change up to 15 MPa. However, the permeability of the lava sample was reduced from 1×10^{-16} m^2 at 2.5 MPa to 1×10^{-17} m^2 at 15 MPa, a decrease of an order of magnitude.

We find that, although the volume of isolated porosity (which ranges between 0.005 and 0.025; i.e., similar to that measured by Michol et al., 2008) does not systematically vary with connected porosity (Fig. 2b), there is an increase therefore in the proportion of isolated porosity as total porosity decreases.

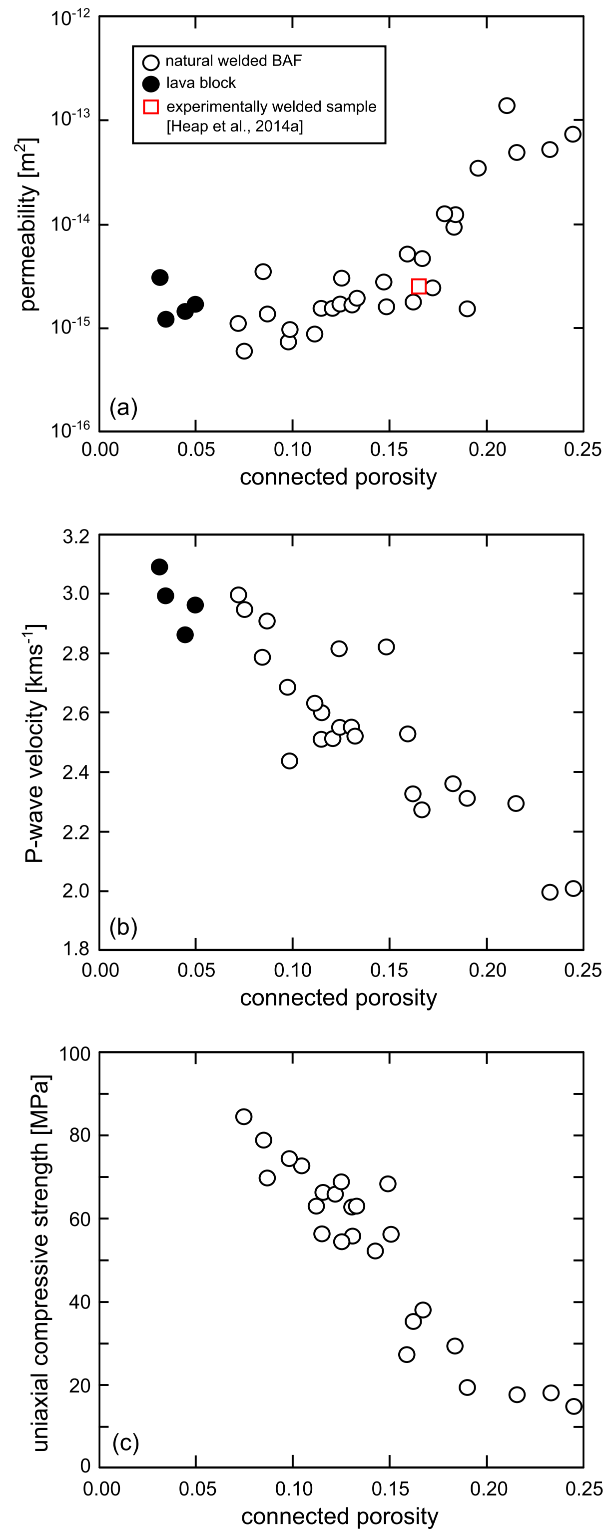

Fig. 1. The impact of viscous densification on physical properties. (a) Permeability as a function of connected porosity. Some of the data (see Tables 2, 3, and 4) are taken from Heap et al. (2014a). (b) P-wave velocity as a function of connected porosity. (c) Uniaxial compressive strength as a function of connected porosity.

4. Discussion

4.1. The evolution of permeability during densification

Previous studies have shown that the permeability of volcanic rock increases nonlinearly as porosity increases (Klug and Cashman, 1996; Saar and Manga, 1999; Rust and Cashman, 2004;

Table 2
Rock physical property summary for the 5 lava samples.

Connected porosity	Total porosity	Isolated porosity	Confining pressure of permeability measurement (MPa)	Permeability (m^2)	P-wave velocity ($km\,s^{-1}$)
0.031	0.046	0.015	1	3.08×10^{-15} [a]	3.09
0.034	0.045	0.011	1	1.22×10^{-15} [a]	2.99
0.040	0.054	0.014	2.5	1.09×10^{-16}	–
			5.0	4.74×10^{-17}	
			7.5	2.99×10^{-17}	
			10.0	2.28×10^{-17}	
			14.9	1.17×10^{-17}	
0.044	0.061	0.017	1	1.48×10^{-15} [a]	2.86
0.050	0.063	0.013	1	1.72×10^{-15} [a]	2.96

[a] Datum taken from Heap et al. (2014a).

Table 3
Rock physical property summary for the 20 welded block-and-ash flow samples containing porosities below the changepoint porosity.

Connected porosity	Total porosity	Isolated porosity	Confining pressure of permeability measurement (MPa)	Permeability (m^2)	P-wave velocity ($km\,s^{-1}$)	Uniaxial compressive strength (MPa)	Pore size estimated using the model of Sammis and Ashby (1986) (μm)
0.072	0.087	0.015	1	1.11×10^{-15} [a]	2.99	–	–
0.075	0.088	0.013	1	6.14×10^{-16} [a]	2.95	84.6	30
0.085	0.097	0.012	1	3.54×10^{-15} [a]	2.79	79.1	31
0.087	0.099	0.012	1	1.38×10^{-15} [a]	2.91	69.7	39
0.098	0.123	0.025	1	9.81×10^{-16} [a]	2.44	–	–
0.098	0.109	0.011	1	7.67×10^{-16}	2.69	74.3	31
0.104	0.112	0.008	–	–	–	72.4	31
0.111	0.121	0.010	1	8.87×10^{-16}	2.63	63.1	39
0.115	0.125	0.010	1	1.55×10^{-15}	2.60	56.7	47
0.115	0.123	0.008	1	1.57×10^{-15}	2.51	66.0	35
0.121	0.129	0.008	1	1.61×10^{-15}	2.51	65.5	34
0.124	0.133	0.009	1	1.73×10^{-15}	2.81	68.9	30
0.125	0.130	0.005	1	3.11×10^{-15}	2.55	54.4	48
0.130	0.137	0.007	–	–	–	55.6	44
0.130	0.136	0.006	1	1.74×10^{-15}	2.55	62.9	34
0.132	0.138	0.006	1	1.90×10^{-15}	2.52	62.8	34
0.142	0.148	0.004	–	–	–	52.0	47
0.147	0.163	0.016	2.5	2.79×10^{-15}	–	–	–
0.148	0.155	0.007	1	1.58×10^{-15}	2.82	68.3	26
0.150	0.161	0.011	–	–	–	55.6	39

[a] Datum taken from Heap et al. (2014a).

Table 4
Rock physical property summary for the 14 welded block-and-ash flow samples containing porosities above the changepoint porosity.

Connected porosity	Total porosity	Isolated porosity	Confining pressure of permeability measurement (MPa)	Permeability (m^2)	P-wave velocity ($km\,s^{-1}$)	Uniaxial compressive strength (MPa)	Pore size estimated using the model of Sammis and Ashby (1986) (μm)
0.165 [b]	0.183	0.018	1	2.64×10^{-15} [a]	2.72	–	–
0.159	0.167	0.008	1	5.29×10^{-15} [a]	2.53	27.0	158
0.162	0.181	0.019	1	1.78×10^{-15} [b]	2.32	35.0	93
0.167	0.182	0.015	1	4.65×10^{-15} [a]	2.27	37.6	78
0.172	0.185	0.013	2.6	2.49×10^{-15}	–	–	–
			5.1	2.49×10^{-15}			
			7.5	2.49×10^{-15}			
			10.0	2.51×10^{-15}			
			14.9	2.51×10^{-15}			
0.179	0.197	0.018	2.5	1.26×10^{-14}	–	–	–
0.183	0.187	0.005	1	9.34×10^{-15} [a]	2.36	29.5	118
0.183	0.201	0.018	2.5	1.22×10^{-14}	–	–	–
0.190	0.215	0.025	1	1.53×10^{-15} [a]	2.31	19.6	259
0.195	0.209	0.014	2.5	3.44×10^{-14}	–	–	–
			5.1	3.57×10^{-14}			
			7.5	3.62×10^{-14}			
			10.0	3.36×10^{-14}			
			15.0	3.58×10^{-14}			
0.210	0.211	0.013	2.5	1.41×10^{-13}	–	–	–
0.215	0.234	0.019	1	4.99×10^{-14} [a]	2.29	15.1	280
0.233	0.246	0.013	1	5.29×10^{-14} [a]	2.00	18.2	254
0.244	0.259	0.015	1	7.27×10^{-14} [a]	2.01	15.1	354

[a] Datum taken from Heap et al. (2014a).
[b] Experimentally welded block-and-ash deposit from Heap et al. (2014a).

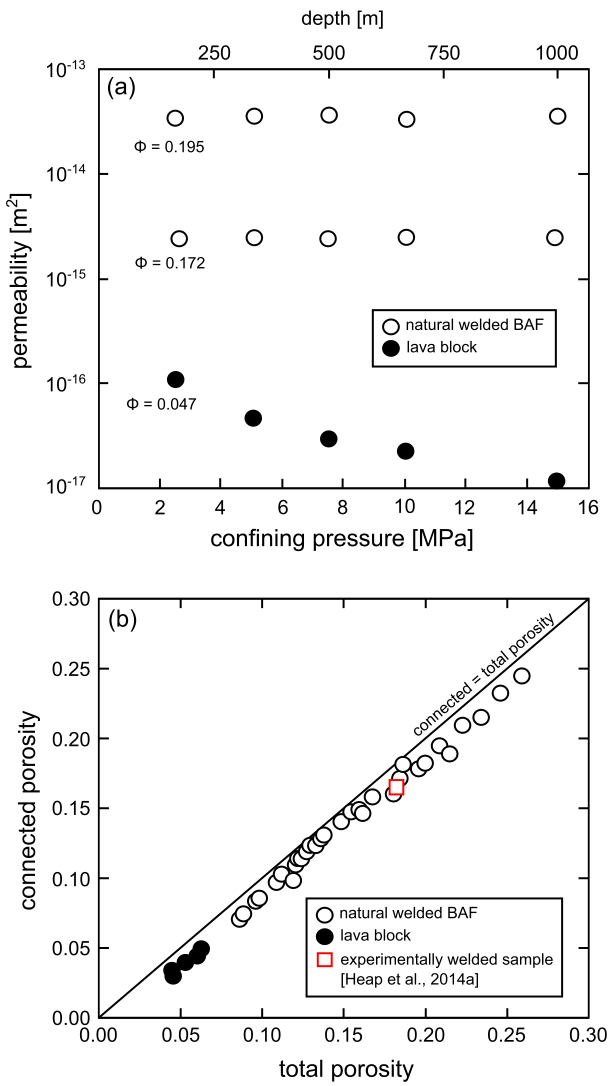

Fig. 2. (a) Permeability as a function of confining pressure (or depth) for two welded block-and-ash flow samples (connected porosity = 0.172 and 0.195) and a lava sample (connected porosity = 0.047). (b) Connected porosity as a function of total porosity. The black line represents the line of connected = total porosity.

Heap et al., 2014b; Farquharson et al., 2015). While many of these studies describe this relationship with a single power law, a recent study (Farquharson et al., 2015) suggested that the porosity–permeability relationship for volcanic rocks can be described by an empirical changepoint model, whereby the data are described by a certain power law permeability–porosity model until a threshold value of porosity (the porosity changepoint), after which the data are best described by a model with a much lower power law exponent (i.e., the porosity–permeability trend is concave down in log–log space). Our study however concerns the evolution of permeability as porosity decreases during viscous densification, rather than the trend during porosity increasing processes such as vesiculation and bubble growth. Thus, we find a very different relationship where the high and low porosity data are described by a high and low power law exponent, respectively (i.e., the porosity–permeability trend is concave up in log–log space; Figs. 1a and 3f).

Recent studies have demonstrated microstructural modifications, influencing pore connectivity, as a governing factor for permeability reduction during viscous densification (Wright and Cashman, 2013; Kendrick et al., 2013; Okumura and Sasaki, 2014; Heap et al., 2014a). The largest pores and channels are closed, restricting fluid flow to tortuous pathways of flattened "crack-like" pores in melt-dominated materials (Wright and Cashman, 2013) or pores sandwiched between crystals in crystal-bearing materials (Heap et al., 2014a). All studies show that densification reduces permeability (Wright and Cashman, 2013; Kendrick et al., 2013; Okumura and Sasaki, 2014; Heap et al., 2014a). Heap et al. (2014a) speculated that there is an abrupt change in the permeability–porosity power law exponent during viscous densification, due to a sudden change in the pore shape and pore volume connectivity. Here we employ a more rigorous method—a modified Bayesian Information Criterion (BIC) method, as described by Main et al. (1999)—to statistically assess whether the permeability decrease can be best described by one or two discrete power law relationships. This approach determines whether increasing the complexity of a model is statistically justifiable when accounting for the additional unknown parameters. The BIC analysis compares two models: linear and piecewise regressions of log-transformed permeability–porosity data, such that:

$$\gamma(x_i) = a_0 + b_0(x_i), \tag{1}$$

and

$$\gamma(x_i) = a_1 + \{b_1 x_i[\forall x_i < x^*]\} + \{x^*(b_1 - b_2) + b_2 x_i[\forall x_i \geq x^*]\}, \tag{2}$$

where $\gamma(x_i)$ is the predicted value of y_i (log-transformed permeability) as a function of x_i (log-transformed porosity), for each iteration i. The linear case includes the intercept a_0 and a single slope b_0, whereas the piecewise model consists of an intercept a_1, a slope b_1 for all values of x_i below the changepoint x^*, and a slope b_2 pertaining to all values of x_i equal to or greater than x^*. The more complex two-slope model can be statistically justified when BIC(x^*)—the maximised information criterion for Equation (2)—is greater that for Equation (1) ($\mathrm{BIC_R}$). We find this to be the case at a changepoint value of $x^* = 1.19$ (equating to a porosity of approximately 0.155), both in terms of the root-mean-square-error and the information criterion analysis (i.e., $\mathrm{BIC}(x^*) > \mathrm{BIC_R}$). Details on the determination and implementation of these criteria are discussed in Main et al. (1999) and Farquharson et al. (2015). Correspondingly, our data is therefore best described by two power law exponents: 8.8 at porosity values above the changepoint porosity and 1.0 below the changepoint (Fig. 3f).

The appearance of a changepoint as porosity decreases below 0.155 can be explained by the evolution of the microstructure during progressive viscous densification (Fig. 3). Above the changepoint, fluids can utilise pores that are as wide as 200–300 μm (Figs. 3c and 3g). Below the changepoint, however, the microstructure is characterised by the absence of large pores (Fig. 3b); the largest pores are typically about 50 μm (Fig. 3d). This observation is supported by pore size analysis of SEM photomicrographs using image processing software ImageJ. Pore diameters were estimated using the average Feret diameter d_F where $d = 3/2(d_F)$ and d is the estimated pore diameter. These data show that there are many pores with a diameter of 150 μm and higher within the sample above the changepoint (Fig. 3h); below the changepoint, there are considerably fewer pores with a diameter above 150 μm (Fig. 3e). The changepoint therefore presumably represents the porosity at which the wide flow channels are efficiently closed, restricting fluid flow to narrower flow paths. The wide flow channels are closed over a small porosity interval and reduce permeability by two orders of magnitude, yielding the relatively high power law exponent above the changepoint. By contrast, a much lower power law exponent describes the permeability–porosity trend below the changepoint: the large number of narrow channels (Figs. 3b and 3e) must be sufficient to allow continued porosity

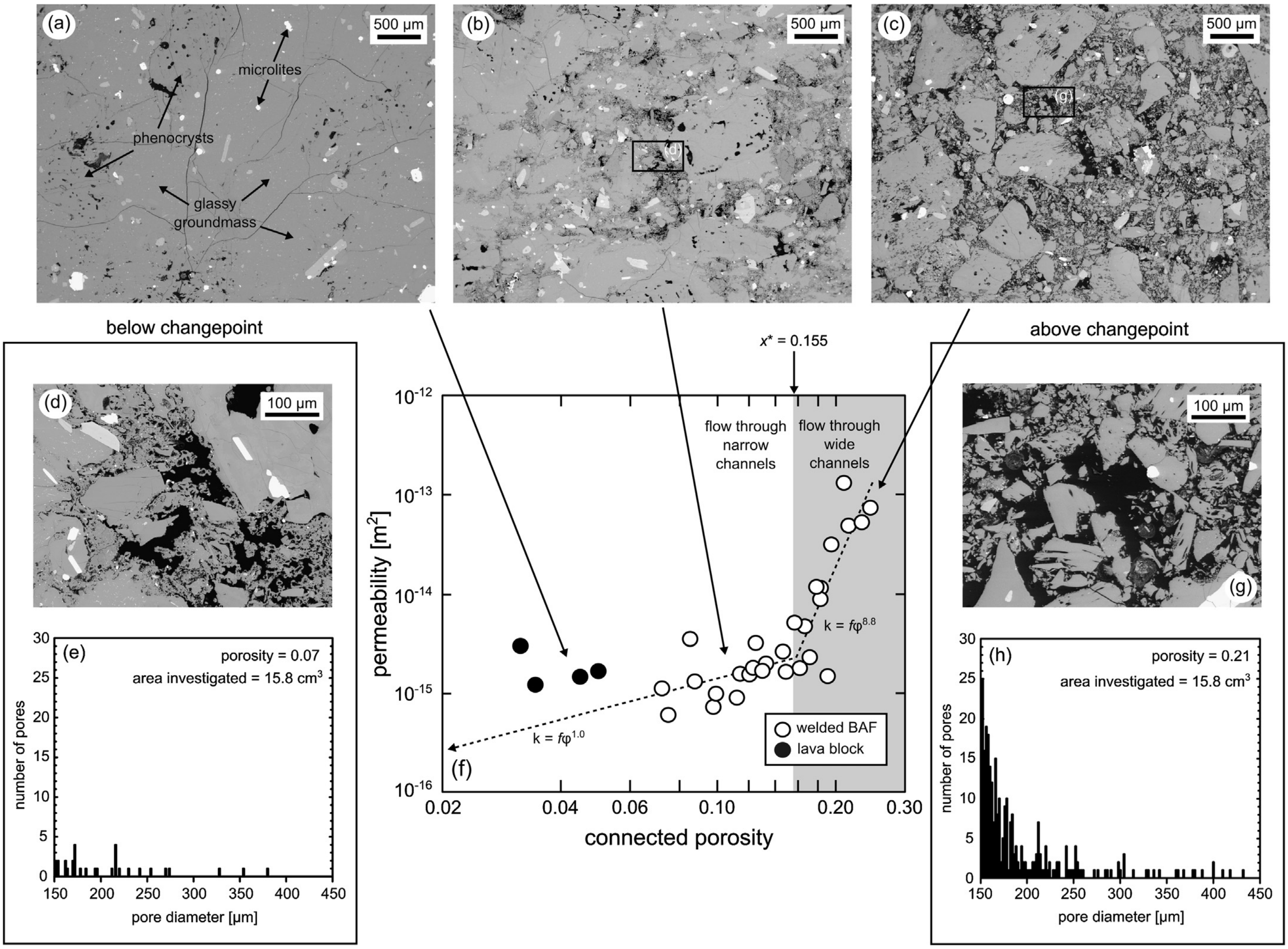

Fig. 3. The evolution of permeability during viscous densification. (a) Back-scattered electron (BSE) photomicrograph of the lava block (the source material). The rock is characterised by phenocrysts (typically 100–400 μm in diameter, but occasionally reaching a couple of mm) within a glassy groundmass containing sparse microlites. (b) BSE photomicrograph of welded block-and-ash flow below the microstructural changepoint. Note that the porosity (in black) is much reduced from the incipiently welded sample in panel (c). We highlight here that the porosity reduction is the result of the sintering and amalgamation of vitric fragments. The largest clast size, where discernible, is on the order of 1–2 mm. (c) BSE photomicrograph of welded block-and-ash flow above the microstructural changepoint. The porosity (in black) is clearly higher than the densely welded sample in panel (b). Many of the vitric shards (up to 1–2 mm in diameter) retain their angular, post-fragmentation shape. (d) BSE photomicrograph showing a zoomed in image of panel (b) to better show the size of the pores below the changepoint. Pores are typically less than 50 μm. (e) Number of pores with a diameter greater than 150 μm within an area of 15.8 cm^2 in the welded block-and-ash flow sample below the microstructural changepoint shown in panel (b). (f) The porosity–permeability data of Fig. 1a with the best-fit slopes provided by the modified Bayesian Information Criterion (BIC) method (see text for details). We provide the relevant power law exponent next to the slopes. The microstructural changepoint (x^*) is also indicated (porosity = 0.155). Above the changepoint fluid flow is assisted by the presence of wide channels (grey zone) and below the changepoint fluid flow is restricted to narrow channels (white zone). (g) BSE photomicrograph showing a zoomed in image of panel (c) to better show the size of the pores above the changepoint. Pores can be as large as 200–300 μm. (h) Number of pores with a diameter greater than 150 μm within an area of 15.8 cm^2 in the welded block-and-ash flow sample above the microstructural changepoint shown in panel (c).

loss without considerable permeability reduction. The permeability of the coherent (i.e., not fragmented and viscously welded) lava samples, not considered in our changepoint analysis, plot above this trend because the connection of the pore network is assisted by a pervasive population of tortuous microcracks (as shown in the SEM photomicrograph of Fig. 3a). This assertion is confirmed by our permeability measurements at elevated pressure (Fig. 2a). When the permeability relies on a network of microcracks, permeability is greatly reduced at low confining pressures due to the ease of microcrack closure at low pressure, a consequence of their high aspect ratio (e.g., Nara et al., 2011). By contrast, the permeability of two welded BAF deposits (porosity 0.172 and 0.195) did not change as the confining pressure increased to 15 MPa (Fig. 2a), indicating that their permeability does not rely on microcracks.

Although the switch from the higher to the lower power law exponent is probably a more gradual transition (e.g., a “change-zone” over a porosity range of 0.14 to 0.17), rather than the discrete changepoint assumed in the model, our data nevertheless show that there exists a microstructurally-controlled break in slope in the permeability–porosity relationship during magma densification. We note that the absolute porosity at which the microstructural changepoint occurs may well be dependent on the initial attributes and textural evolution (e.g., crystal content, grain and crystal size distribution, degree of strain, amongst others) of the granular material during densification. Here therefore we only consider materials with polydisperse grain size distributions; further work is likely required to parameterise the changepoint, or the existence of a changepoint, for different volcanic materials.

The timescales for the viscous densification of volcanic materials have been discussed by several authors (e.g., Quane et al., 2009; Kolzenburg and Russell, 2014; Heap et al., 2014a; Okumura and Sasaki, 2014). The study of Heap et al. (2014a) used the rheological model of Russell and Quane (2005),

$$\Delta t = \frac{\eta_0(1-\phi^i)}{\alpha\sigma}\left[\exp\left(\frac{-\alpha\phi}{1-\phi}\right) - \exp\left(\frac{-\alpha\phi^i}{1-\phi^i}\right)\right], \quad (3)$$

to estimate densification timescales using data from high temperature viscous welding experiments conducted on disaggregated glassy material from the Mount Meager welded BAF deposit (i.e., the same materials used in the present study). Here η_o is the effective viscosity of the melt plus crystal cargo at zero porosity (extrapolated from the experimental data of Heap et al., 2014a), α is a dimensionless empirical coefficient (equal to 2, as determined from the experiments of Heap et al., 2014a), σ is the lithostatic (or "magmastatic") stress acting on the deposit, ϕ is the time-dependent porosity, and ϕ^i is the initial porosity of the deposit (taken here to be 0.4, a typical porosity for polydisperse granular materials close to their maximum packing, see Heap et al., 2014a). The applicability of this model for our permeability data is highlighted by the coincidence between the permeability of the natural samples and that of the viscously welded experimental sample used for the determination of η_o and α (the unfilled square in Figs. 1a and 2b; see Heap et al., 2014a). First, we modelled the porosity loss with time for melt viscosities at three temperatures (800, 900, and 1000 °C; using the temperature dependence of the melt viscosity from Heap et al., 2014a) and a stress of 3.75 MPa (corresponding to a depth of 250 m; estimated as before using $\sigma = \rho gh$) (Fig. 4a). To demonstrate the influence of depth on viscous porosity loss, we provide an additional curve for 800 °C and 750 m. Our permeability data measured at 1 MPa are likely to also represent those at the depths implicated here: we note that the permeability of the welded BAF samples does not decrease up to confining pressures of 15 MPa (corresponding to depths of 1000 m) (Fig. 2a). We find that the rate of porosity decrease is very much dependent on the stress/depth and viscosity/temperature (see also Quane et al., 2009; Kolzenburg and Russell, 2014; Heap et al., 2014a). For example, the time to halve the porosity (i.e., to reach a porosity of 0.2) is 19 and 5 days for temperatures of 800 and 900 °C, respectively (for a depth of 250 m). As depth is increased from 250 to 750 m (at a constant temperature of 800 °C), the time required to reach a porosity of 0.2 is reduced from 19 to 6.5 days. Using these modelled porosity curves, we can plot the time required to densify to the changepoint (i.e., a porosity of 0.155—the porosity at which flow is no longer aided by wide flow channels—corresponding to a permeability of 2.1×10^{-15} m^2) (Fig. 4b). We do this by inserting a constant porosity of 0.155 into Equation (3) and computing the values of Δt for all values of η_0 (which in turn correspond to values of temperature). At a temperature of 900 °C it takes 6 and 2 days to reach the changepoint at depths of 250 and 750 m, respectively (Fig. 4b). In other words, at a starting porosity of 0.4, permeability can be reduced by about four orders of magnitude in timescales from days to weeks. Using the power laws defined by our changepoint model (Fig. 3f), and the modelled evolution of porosity with time (Fig. 4a), we can predict the evolution of permeability with time for different temperatures and depths (Fig. 4c). The rate of permeability decrease is very much dependent on the stress/depth, viscosity/temperature, and time. It takes 24 days at a temperature of 800 °C and a depth of 250 m to reduce the permeability from 1×10^{-11} to 2×10^{-15} m^2 (i.e., the changepoint), but a further 16 days to reduce the permeability by an additional order of magnitude (i.e., to 2×10^{-16} m^2). At 750 m, these times are reduced to 8 and 5 days, respectively (Fig. 4c). These permeability reduction timescales are much larger than those estimated by Okumura and Sasaki (2014) for crystal-free melts (100 to 1000 s), highlighting the significant impact of crystals on permeability reduction timescales, a consequence of their large influence on the effective viscosity (e.g., Andrews et al., 2014; Heap et al., 2014a).

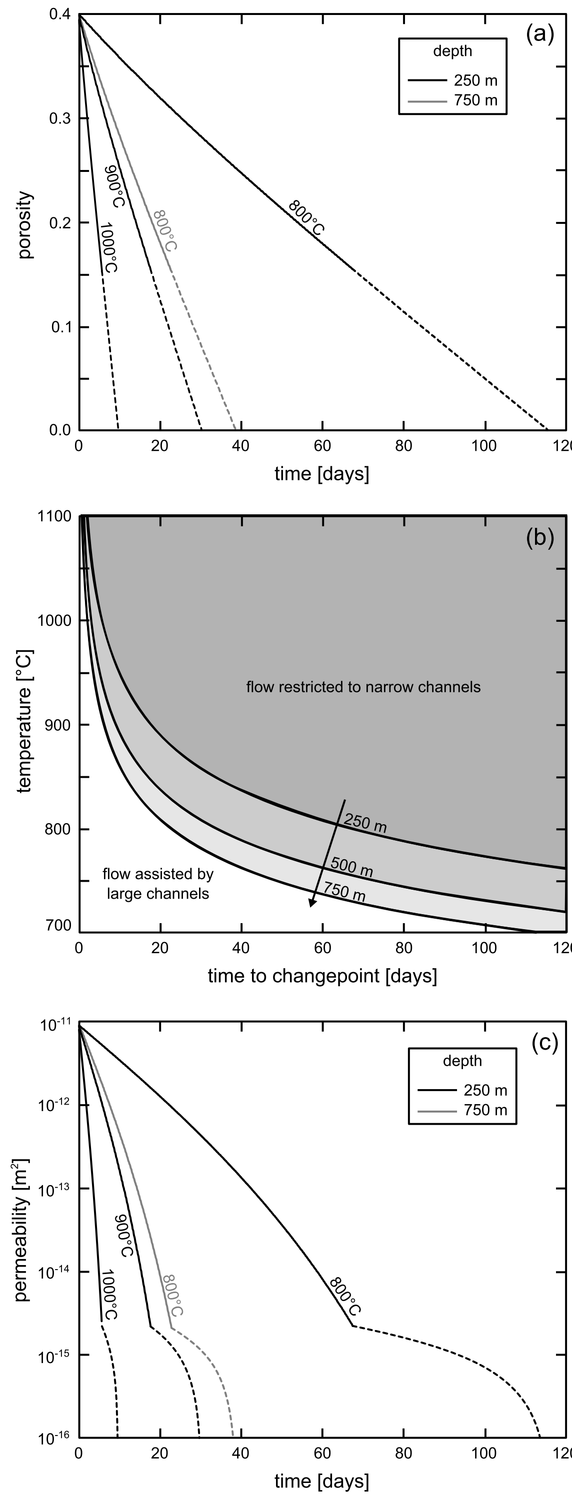

Fig. 4. (a) Compaction timescales. Modelled porosity-time curves using the rheological model of Russell and Quane (2005) (Equation (3)) for melt viscosities at three temperatures (800, 900, and 1000 °C) and lithostatic stresses of 3.75 and 11.25 MPa (depths corresponding to 250 and 750 m, respectively; see text for details). (b) Curves showing the time required to reach the microstructural changepoint (porosity = 0.155) as a function of temperature for different depths (250–750 m). (c) Permeability reduction timescales. Modelled permeability-time curves (using the modelled output of Fig. 4a and the discrete power law permeability–porosity relationships defined by the changepoint model) for melt viscosities at three temperatures (800, 900, and 1000 °C) and lithostatic stresses of 3.75 and 11.25 MPa (depths corresponding to 250 and 750 m, respectively; see text for details). The curves are dashed below the changepoint porosity in panels (a) and (b) because the model may not accurately capture the porosity evolution due to the change in pore geometry.

4.2. The evolution of P-wave velocity and uniaxial compressive strength during densification

The data of this study show that P-wave velocity and strength increase as porosity decreases (Figs. 1b and 1c), behaviour consistent with previous experimental studies on rocks (e.g., Chang et al., 2006) and viscously welded materials (Vasseur et al., 2013). The linear increase of P-wave velocity with decreasing porosity is not influenced by the microstructural changepoint; it is likely that the closure of the largest pores does not influence the first arrival (elastic wave velocities are much more sensitive to void space with a high aspect ratio, like cracks; O'Connell and Budiansky, 1974). However, the strength data (Fig. 1c) show a break in slope at approximately the same position as the microstructural changepoint (porosity = 0.155). The strength of rocks is not only a function of porosity, but very much depends on the pore size (Vasseur et al., 2013; Heap et al., 2014c). An explanation for the mechanical behaviour of these materials therefore requires a model that considers both porosity and pore size, such as the pore-emanating crack model of Sammis and Ashby (1986). Sammis and Ashby's (1986) micromechanical model has successfully described the mechanical behaviour of volcanic materials (e.g., Zhu et al., 2011; Vasseur et al., 2013). The model describes a two-dimensional elastic medium populated by circular holes of uniform radius r. Cracks emanate from the circular holes (parallel to the direction of the applied stress) when the stress at the tip of a small crack on the circular surface reaches a critical value (the fracture toughness, K_{IC}). The newly-formed cracks propagate to a distance l in the direction of the maximum principal stress. The cracks interact when they reach a certain length, thus increasing the local tensile stress intensity. Eventually, the coalescence of these cracks induces the macroscopic failure of the elastic medium. In the case of uniaxial compression, Zhu et al. (2010) derived an analytical approximation of Sammis and Ashby's (1986) pore-emanating crack model to estimate the uniaxial compressive strength (σ_p) as a function of the porosity (ϕ):

$$\sigma_p = \frac{1.325}{\phi^{0.414}} \frac{K_{IC}}{\sqrt{\pi r}}. \tag{4}$$

If the pore-emanating cracks grow through the particles, the value of K_{IC} would closely resemble the values of the mineral constituents: $K_{IC} = 0.3$–0.4 MPa m$^{0.5}$ for feldspar (Atkinson and Meredith, 1987) and $K_{IC} = 0.7$ MPa m$^{0.5}$ for glass (borosilicate glass; Wiederhorn, 1969). However, cracks are likely to grow along particle boundaries that will serve to significantly lower K_{IC} (Atkinson and Meredith, 1987). For example, the K_{IC} of a tuff from the Alban Hills (Italy) was estimated to be 0.1–0.2 MPa m$^{0.5}$ as a result of cracks growing along weak clast interfaces (Zhu et al., 2011). If we assume an intermediate $K_{IC} = 0.15$ MPa m$^{0.5}$, curves of uniaxial compressive strength against porosity can be modelled for different pore diameters, as in Fig. 5a. We find that the strength of the samples below the changepoint can be described by a single characteristic pore size (= 40 μm). However, there is no unique curve for the data above the changepoint, the model suggests that the pore size is decreasing (from 300 to 40 μm; Fig. 5a) as porosity is reduced to the changepoint. This is best observed when the pore size is calculated for each experiment using Equation (4) ($K_{IC} = 0.15$ MPa m$^{0.5}$), as shown in Fig. 5b. The model predicts that the pore size is reduced from ∼350 μm at a porosity of 0.25 to a pore size of ∼50 μm at the changepoint porosity (= 0.155). The pore size does not change as porosity is decreased below 0.155 (Fig. 5b). These predicted pore diameters are in close agreement with our microstructural observations and quantitative pore size analysis (Fig. 3) and therefore add rigour to our above interpretation of the changepoint (i.e., wide channels are progressively closed above the changepoint, while the numerous narrow channels below the changepoint allow porosity loss without considerable permeability reduction).

As discussed, strength versus porosity below the changepoint is well described by Equation (4) using a constant pore size of 40 μm. However, we can also compute the strength above the changepoint using Equation (4) by calculating pore size using the slope of pore size change with decreasing porosity to the changepoint (which is approximately linear; Fig. 5b). These modelled curves are presented in Fig. 5c. The models of strength increase with decreasing porosity above and below the changepoint can then be used in conjunction with the rheological compaction model (Equation (3)) to provide timescales of strength increase during magma densification (Fig. 5d). The rate of strength increase is very much dependent on the stress/depth, viscosity/temperature, and time. It takes 24.5 days at a temperature of 800 °C and a depth of 250 m to increase the strength from ∼8 to ∼56 MPa, but only a further 13 days to almost double the strength to ∼100 MPa. At 750 m, these times are reduced to 8 and 4.5 days, respectively (Fig. 5d).

Although we report uniaxial compressive strengths here (this is a standard way to assess strength and allows us to use models optimised for uniaxial compressive strengths, such as the Sammis and Ashby, 1986 model), we highlight that the fracture of magma is more likely to occur in either shear (e.g., Cordonnier et al., 2012) or in tension (e.g., Heiken et al., 1988). Further, we highlight that the model assumes that the pores are circular and may not therefore capture the behaviour of compacted deposits containing pores with a high aspect ratio (which may be the case for highly-sheared and/or melt-dominated materials; e.g., Wright and Cashman, 2013).

5. Densification, permeability reduction, and strength recovery in volcanic environments

The permeability and strength data and modelling presented herein are relevant to the viscous densification of porous, polydisperse granular materials of crystal-bearing melts in the absence of significant differential/shear stresses.

Lava dome extrusion at the surface is often accompanied by repetitive, low-magnitude and low-frequency earthquakes at depth (e.g., Neuberg et al., 2006), considered to be the result of magma fracture (e.g., Tuffen et al., 2003; Thomas and Neuberg, 2012) or slip events on fractures containing shards of juvenile material (Tuffen and Dingwell, 2005). Preserved and extruded examples of these fractures expose them to be filled with fragmented ash shards, and they are thought to play a key—albeit transient—role in the outgassing of magmatic volatiles through the edifice or into the permeable country rock (e.g., Stasiuk et al., 1996; Rust et al., 2004; Kolzenburg et al., 2012; Castro et al., 2014). Such transient channels in highly viscous magma help to bleed the overpressure that is generated by gas exsolution in silicic volcanic conduits (e.g., Gonnermann and Manga, 2007) and complicate eruptive scenarios such that both explosive and effusive behaviour can be coincident at the same vent (e.g., Woods and Koyaguchi, 1994; Schipper et al., 2013). Once formed, the permeability of these fragment-filled fractures, and their strength recovery, may be approximated using the simple model presented in this study (provided that the material remains hot; we note that some the fractures may propagate to significant distances into the country rock (Heiken et al., 1988), allowing the fragmental fracture fill to cool below its glass transition temperature). The modelled changes in strength and permeability with time are plotted together in Fig. 6, for an isothermal melt viscosity at 800 °C and a lithostatic stress of 11.25 MPa (i.e., a depth of 750 m). Fig. 6 shows that the strength increase after 6 days is only a factor of two; the permeability change over the same timeframe is more than two orders of magnitude. As magma near the conduit margin ascends through regions that sat-

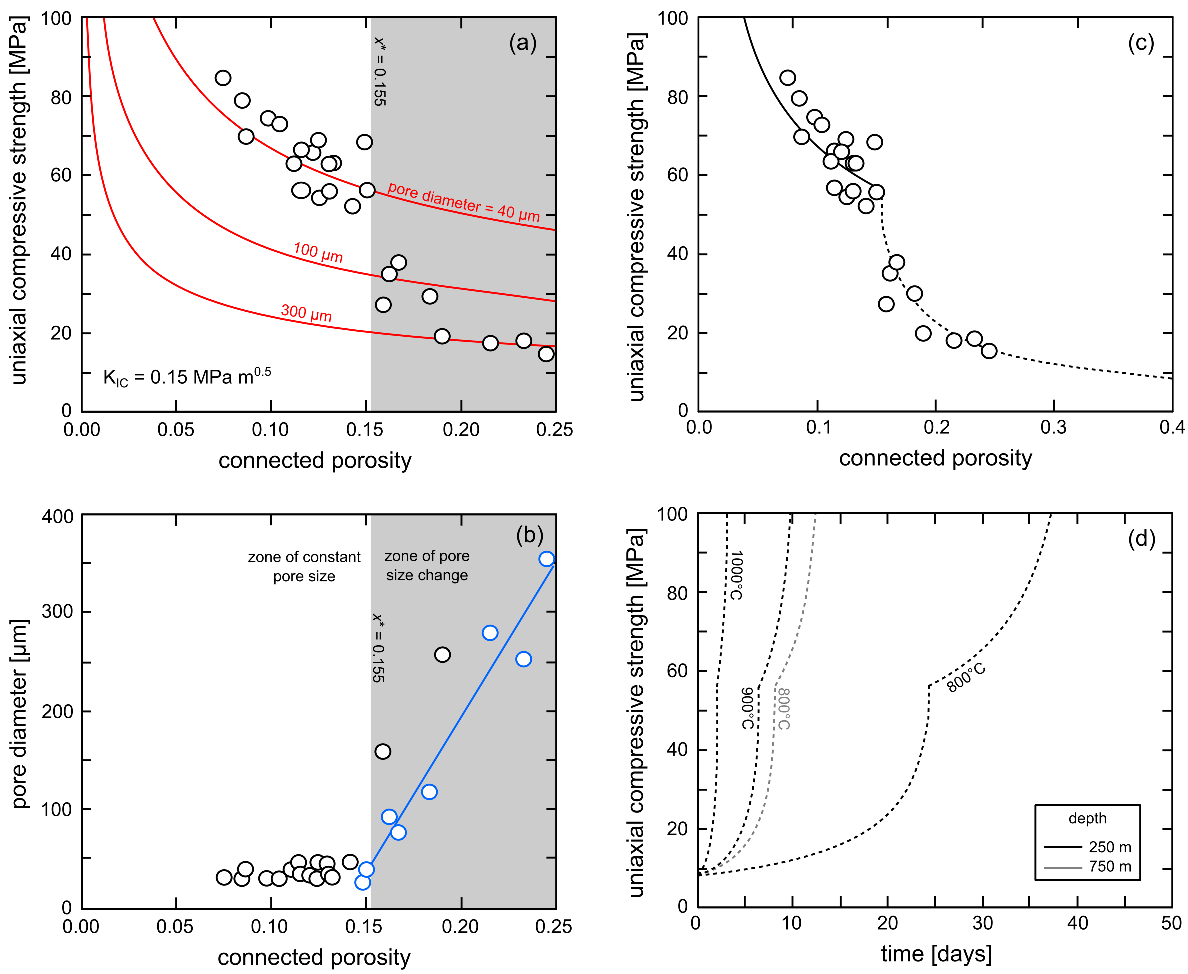

Fig. 5. (a) Micromechanical modelling. Uniaxial compressive strength as a function of connected porosity (the data of Fig. 1c) plotted with the modelled curves, for different pore diameters, from Sammis and Ashby's pore-emanating crack model (Equation (4); using $K_{IC} = 0.15$ MPa m$^{0.5}$). The microstructural changepoint (x^*) is also indicated (porosity = 0.155). (b) Pore size as a function of porosity. Pore diameters were calculated using Sammis and Ashby's pore-emanating crack model (Equation (4); using $K_{IC} = 0.15$ MPa m$^{0.5}$). The blue data highlight those used to determine the pore size change with decreasing porosity to the changepoint; the blue curve represents a linear fit through those data. The microstructural changepoint (x^*) is also indicated (porosity = 15.5%). (c) Uniaxial compressive strength as a function of connected porosity. The panel shows the experimental data of Fig. 1a together with curves modelled using the Sammis and Ashby (1986) pore-emanating crack model. A pore diameter of 40 μm is used below the changepoint, and a pore diameter that changes as a function of porosity (see panel (b)) is used above the changepoint (Equation (4); using $K_{IC} = 0.15$ MPa m$^{0.5}$). The curves are dashed above the changepoint porosity because the pore sizes used to calculate the curve were determined using Sammis and Ashby's (1986) model (see panel (b) and text for details). (d) Strength increase timescales. Modelled strength-time curves (using the modelled output of Fig. 4a and the strength-porosity models shown in panel (c)) for melt viscosities at three temperatures (800, 900, and 1000 °C) and lithostatic stresses of 3.75 and 11.25 MPa (depths corresponding to 250 and 750 m, respectively; see text for details). The curves are dashed below the changepoint porosity because the viscous compaction model may not accurately capture the porosity evolution due to the change in pore geometry, and above the changepoint porosity because the pore sizes used to calculate the curve were determined using Sammis and Ashby's (1986) model (see panel (b) and text for details). (For interpretation of the references to color in this figure legend, the reader is referred to the web version of this article.)

isfy the criteria for fracturing (e.g., Gonnermann and Manga, 2003; Thomas and Neuberg, 2012), the relatively long timescales required for permeability reduction (Fig. 6) may keep the edges of the conduit sufficiently permeable to facilitate outgassing into the country rock (e.g., Shields et al., 2014), or via a permeable halo surrounding the conduit (e.g., Rust et al., 2004). The repeat times between successive low-magnitude and low-frequency earthquakes during silicic lava dome extrusion (from minutes to hours, see Tuffen et al., 2003 and references therein) suggest that magma re-fracturing takes place long before permeability can decrease, keeping the conduit margin permeable (see inset on Fig. 6). The ease of magma re-fracturing is supported here by our estimates of the timescales of strength recovery, which are much greater than our permeability reduction timescales. We further note that magma re-fracturing may be assisted by small (0.5 MPa) pore overpressures (Heap et al., 2015); increased pore fluid pressures are thought to transiently occur in magma fractures (Castro et al., 2014). To conclude, any repetition of fracturing events likely occurs prior to significant increases in strength and must therefore occur more frequently than the viscous densification timescale (as argued in Tuffen and Dingwell, 2005).

We note here that, melt viscosity may decrease, and the viscous densification timescales lowered, if exsolved volatiles passing through the fractured magma can be reabsorbed into the melt phase (Sparks et al., 1999). However, we highlight that the ratio of the timescales of strength recovery and permeability reduction (i.e., that the timescale for strength recovery is longer than that for permeability reduction) will be independent of effective viscosity and imposed stress. We further note that stresses additional to that of the lithostatic (e.g., the high shear stresses anticipated close to the conduit margin; Gonnermann and Manga, 2003), not considered in our simple model, may accelerate densification and reduce the timescales required for permeability decrease and strength increase. However, while in-conduit densification is expected to be accelerated by significant shear stresses driving shear strain, significant pore fluid pressure can retard densification. This is especially

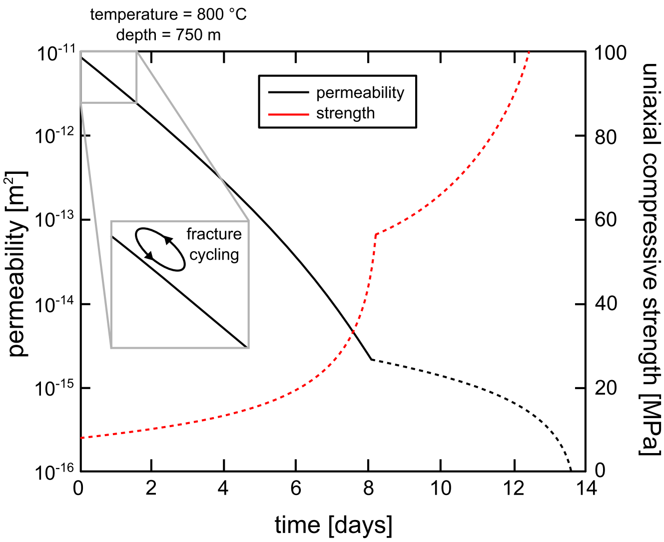

Fig. 6. Permeability reduction and strength increase timescales for the melt viscosity at 800 °C and a lithostatic stress of 11.25 MPa (or a depth of 750 m; see text for details). The permeability-time curve was modelled using the output of Fig. 4a and the discrete power law permeability–porosity relationships defined by the changepoint model (Fig. 3f). The strength-time curve was modelled using the output of Fig. 4a and the strength-porosity models shown in Fig. 5c. The curves are dashed below the changepoint porosity because the model may not accurately capture the porosity evolution due to the change in pore geometry. The strength increase curve is also dashed above the changepoint porosity because the pore sizes used to calculate the curve were determined using Sammis and Ashby's (1986) model. Inset shows a zoom of the start of the permeability reduction curve showing the permeability evolution of conduit margin fractures based on re-fracture timescales provided by low-magnitude and low-frequency earthquakes during silicic lava dome extrusion (from minutes to hours, see Tuffen et al., 2003 and references therein).

true in the volumetric pressure case where densification will halt when the hydrostatic pressure matches the pore fluid pressure. As mentioned above, increased pore fluid pressures are thought to occur, albeit transiently, in particle-filled fractures within magma (e.g., Castro et al., 2014). It is clear that much experimental and theoretical work is required on the viscous densification of granular magma in various stress regimes to facilitate this discussion.

The conduit zone of Unzen volcano (Japan) chiefly comprises volcanic breccia, as revealed by the cores recovered from the 2003–2004 Unzen Scientific Drilling Project (Goto et al., 2008). This conduit-filling breccia is thought to have formed during the growth of the edifice through the disintegration of previous infill material and wall rocks by explosive eruptions and gravitational failures, a model considered applicable to other polygenetic volcanoes developed through explosive followed by effusive behaviour (Goto et al., 2008). Other examples of polydisperse granular conduit fill include: pyroclastic shallow conduit infill at Mount Meager (Canada) (Kolzenburg and Russell, 2014) and Shiotani (Japan) (Kano et al., 1997) following an explosive eruption, the rheomorphic flow of densified pyroclastic material back into the vent at Las Cañadas caldera, Tenerife (Canary Islands) (Soriano et al., 2009), and intra-caldera brecciation at Scafell caldera (Lake District, England) as a result of subaerial caldera collapse (Branney and Kokelaar, 1994). The permeability reduction and strength recovery of these conduit-filling deposits may be approximated using the modelling of the present study (Figs. 4c, 5d and 6). For example, the reduction in permeability may restrict the efficiency with which gases can escape up through the conduit (within days to weeks; e.g., Edmonds et al., 2003; Nicholson et al., 2013). If pore pressure builds as a result of the permeability reduction, the conditions preparatory to a subsequent explosive eruption may be satisfied (e.g., Melnik et al., 2005; Diller et al., 2006). However, the relatively slow initial increase in strength during viscous densification (Fig. 6) coupled with the fact that pore overpressures drastically reduce strength (Heap et al., 2015) may facilitate magma fracturing within the conduit—as seen in the conduit-filling breccia of Unzen volcano (Goto et al., 2008)—thus providing pathways for the lateral outgassing of magmatic volatiles.

The results of this study may therefore provide support for models of conduit outgassing (e.g., Collinson and Neuberg, 2012).

6. Concluding remarks

Transitions between effusive and explosive behaviour are commonplace at many active volcanoes. If the outgassing efficiency, controlled by the permeability of the system, exerts a crucial control on eruption style, then a constantly changing permeability may be responsible for the observed fluctuations in eruption style. Our study highlights that the progressive densification of magma by viscous sintering during dome-building extrusion, driven by the load provided by the magmatic column, will decrease the porosity and permeability and increase the strength of conduit magma and ash-filled fractures that form at the conduit margin. The viscous magma densification will therefore inhibit outgassing efficiency over time. However, the slow strength recovery of densifying ash-filled fractures, shown herein, suggests that conduit margin fractures may continually re-fracture and remain permeable, allowing the conduit to outgas into the edifice rock and up through the damage zone enveloping the conduit. Therefore, the permeability and outgassing efficiency of the system will depend on the competition between permeability reduction within the conduit and outgassing through conduit margin fractures. If fluid escape can be ultimately disrupted, pore pressure will increase and, if pore pressure increases sufficiently, the conditions required to switch from effusive to explosive (e.g., Vulcanian eruptions) behaviour may be realised. An explosive episode will then reset the magma densification clock, and the process will start again. The timescales of permeability reduction and strength recovery in densifying magma presented in this study may aid our understanding of, amongst others, surface outgassing cycles, magma fracture-healing cycles, and the timescales required for pore pressure augmentation and the initiation of explosive eruptions.

Acknowledgements

We warmly thank James Welles, Amy Ryan, Michelle Campbell, Thierry Reuschlé, and Patrick Baud. Gilles Morvan is thanked for his assistance using the SEM, and Alex Kushnir for discussions during the SEM session. We would also like to thank Joern Unger, Doug Polson, and David Jones for technical assistance at the Volcanology and Petrology Laboratory (UBC) during development of the UBC experimental setup. M.J. Heap and J.I. Farquharson acknowledge an Initiative d'Excellence (IDEX) "Attractivité" grant (VOLPERM) and an IDEX "Contrats doctoraux" grant, respectively, both funded by the University of Strasbourg. Funding for F.B. Wadsworth was provided by the European Union's Seventh Programme for research, technological development, and demonstration under grant agreement No. 282759 (VUELCO). S. Kolzenburg was funded by a Compagnia San Paulo grant and an UNITO (EX 60%) local research project. J.K. Russell acknowledges funding from the NSERC Discovery and Discovery Accelerator Supplements programs (No. 15841). The authors of this study also acknowledge a Hubert Curien Partnership (PHC) Procope grant (grant number 332065SG in France and 57130387 in Germany) funded and implemented by the Deutscher Akademischer Austauschdienst (DAAD) in Germany, and the Ministry of Foreign Affairs (MAEDI) and the Ministry of Higher Education and Research (MENESR) in France. This paper was improved following the constructive comments of Hugh Tuffen, one anonymous reviewer, and the editor, Tamsin Mather.

References

Andrews, G.D.M., Russell, J.K., Stewart, M.I., 2014. The history and dynamics of a welded pyroclastic dam and its failure. Bull. Volcanol. 76, 811.

Atkinson, B.K., Meredith, P.G., 1987. Experimental fracture mechanics data for rocks and minerals. In: Atkinson, B.K. (Ed.), Fracture Mechanics of Rock. Academic Press, London, pp. 477–525.

Blower, J., 2001. Factors controlling permeability–porosity relationships in magma. Bull. Volcanol. 63, 497–504.

Branney, M.J., Kokelaar, B.P., McConnell, B.J., 1992. The Bad Step Tuff: a lava-like rheomorphic ignimbrite in a calc-alkaline piecemeal caldera, English Lake District. Bull. Volcanol. 54, 187–199.

Branney, M.J., Kokelaar, B.P., 1994. Volcanotectonic faulting, soft-state deformation, and rheomorphism of tuffs during development of a piecemeal caldera, English Lake District. Bull. Geol. Soc. Am. 106, 507–530.

Castro, J., Bindeman, I.N., Tuffen, H., Schipper, C.I., 2014. Explosive origin of silicic lava: textural and δD–H_2O evidence for pyroclastic degassing during rhyolite effusion. Earth Planet. Sci. Lett. 405, 52–61.

Chang, C., Zoback, M.D., Khaksar, A., 2006. Empirical relations between rock strength and physical properties in sedimentary rocks. J. Pet. Sci. Eng. 51, 223–237.

Collinson, A.S.D., Neuberg, J., 2012. Gas storage, transport and pressure changes in an evolving permeable volcanic edifice. J. Volcanol. Geotherm. Res. 243–244, 1–13.

Cordonnier, B., Caricchi, L., Pistone, M., Castro, J., Hess, K.-U., Gottschaller, S., Manga, M., Dingwell, D.B., Burlini, L., 2012. The viscous-brittle transition of crystal-bearing silicic melt: direct observation of magma rupture and healing. Geology 40, 611–614.

Diller, K., Clarke, A.B., Voight, B., Neri, M., 2006. Mechanisms of conduit plug formation: implications for vulcanian explosions. 33, 20. http://dx.doi.org/10.1029/2006GL027391.

Edmonds, M., Oppenheimer, C., Pyle, D.M., Herd, R.A., Thompson, G., 2003. SO_2 emissions from Soufrière Hills Volcano and their relationship to conduit permeability, hydrothermal interaction and degassing regime. J. Volcanol. Geotherm. Res. 124, 23–43.

Eichelberger, J.C., Carrigan, C.R., Westrich, H.R., Price, P.H., 1986. Non-explosive silicic volcanism. Nature 323, 598–602.

Farquharson, J.I., Heap, M.J., Varley, N., Baud, P., Reuschlé, T., 2015. Permeability and porosity relationships of edifice-forming andesites: a combined field and laboratory study. J. Volcanol. Geotherm. Res. 297, 52–68.

Gonnermann, H.M., Manga, M., 2003. Explosive volcanism may not be an inevitable consequence of magma fragmentation. Nature 426, 432–435.

Gonnermann, H.M., Manga, M., 2007. The fluid mechanics inside a volcano. Annu. Rev. Fluid Mech. 39, 321–356.

Goto, Y., Nakata, S., Kurokawa, M., Shimano, T., Sugimoto, T., Sakuma, S., Hoshizumi, H., Yoshimoto, M., Uto, K., 2008. Character and origin of lithofacies in the conduit of Unzen volcano, Japan. J. Volcanol. Geotherm. Res. 175, 45–59.

Grunder, A., Russell, J.K.R., 2005. Welding processes in volcanology: insights from field, experimental, and modeling studies. J. Volcanol. Geotherm. Res. 142, 1–9.

Heap, M.J., Kolzenburg, S., Russell, J.K., Campbell, M.E., Welles, J., Farquharson, I.J., Ryan, A., 2014a. Conditions and timescales for welding block-and-ash flow deposits. J. Volcanol. Geotherm. Res. 289, 202–209.

Heap, M.J., Lavallée, Y., Petrakova, L., Baud, P., Reuschlé, T., Varley, N., Dingwell, D.B., 2014b. Microstructural controls on the physical and mechanical properties of edifice-forming andesites at Volcán de Colima, Mexico. J. Geophys. Res. 119, 2925–2963.

Heap, M.J., Xu, T., Chen, C.-f., 2014c. The influence of porosity and vesicle size on the brittle strength of volcanic rocks and magmas. Bull. Volcanol. 76, 856. http://dx.doi.org/10.1007/s00445-014-0856-0.

Heap, M.J., Xu, T., Kushnir, A.R.L., Kennedy, B., Chen, C.-f., 2015. Fracture of magma containing overpressurised pores. J. Volcanol. Geotherm. Res. 301, 180–190.

Heiken, G., Wohletz, K., Eichelberger, J.C., 1988. Fracture fillings and intrusive pyroclasts, Inyo Domes, California. J. Geophys. Res. 93, 4335–4350.

Kano, K., Matsuura, H., Yamauchi, S., 1997. Miocene rhyolitic welded tuff infilling a funnel-shaped eruption conduit Shiotani, southeast of Matsue, SW Japan. Bull. Volcanol. 59, 125–135.

Kendrick, J.E., Lavallée, Y., Hess, K.-U., Heap, M.J., Gaunt, H.E., Meredith, P.G., Dingwell, D.B., 2013. Tracking the permeable porous network during strain-dependent magmatic flow. J. Volcanol. Geotherm. Res. 260, 117–126.

Klug, C., Cashman, K.V., 1996. Permeability development in vesiculating magmas: implications for fragmentation. Bull. Volcanol. 58, 87–100.

Kolzenburg, S., Heap, M.J., Lavallée, Y., Russell, J.K., Meredith, P.G., Dingwell, D.B., 2012. Strength and permeability recovery of tuffisite-bearing andesite. Solid Earth 3, 191–198.

Kolzenburg, S., Russell, J.K., 2014. Welding of pyroclastic conduit infill: a mechanism for cyclical explosive eruptions. J. Geophys. Res. 119, 5305–5323.

Main, I.G., Leonard, T., Papasouliotis, O., Hatton, C.G., Meredith, P.G., 1999. One slope or two? Detecting statistically significant breaks of slope in geophysical data, with application to fracture scaling relationships. Geophys. Res. Lett. 26, 2801–2804.

Mellors, R.A., Sparks, R.S.J., 1991. Spatter-rich pyroclastic flow deposits on Santorini, Greece. Bull. Volcanol. 53, 327–342.

Melnik, O., Barmin, A.A., Sparks, R.S.J., 2005. Dynamics of magma flow inside volcanic conduits with bubble overpressure buildup and gas loss through permeable magma. J. Volcanol. Geotherm. Res. 143, 53–68.

Michol, K.A., Russell, J.K.R., Andrews, G.D.M., 2008. Welded block and ash flow deposits from Mount Meager, British Columbia, Canada. J. Volcanol. Geotherm. Res. 169, 121–144.

Nara, Y., Meredith, P.G., Yoneda, T., Kaneko, K., 2011. Influence of macro-fractures and micro-fractures on permeability and elastic wave velocities in basalt at elevated pressure. Tectonophysics 503, 52–59.

Neuberg, J.W., Tuffen, H., Collier, L., Green, D., Powell, T., Dingwell, D.B., 2006. The trigger mechanism of low-frequency earthquakes on Montserrat. J. Volcanol. Geotherm. Res. 153, 37–50.

Nicholson, E.J., Mather, T.A., Pyle, D.M., Odbert, H.M., Christopher, T., 2013. Cyclical patterns in volcanic degassing revealed by SO_2 flux timeseries analysis: an application to Soufrière Hills Volcano, Montserrat. Earth Planet. Sci. Lett. 375, 209–221.

O'Connell, R.J., Budiansky, B., 1974. Seismic velocities in dry and saturated cracked solids. J. Geophys. Res. 79, 5412–5426.

Okumura, S., Sasaki, O., 2014. Permeability reduction of fractured rhyolite in volcanic conduits and its control on eruption cyclicity. Geology 42, 843–846.

Quane, S.L., Russell, J.K., Friedlander, E.A., 2009. Time scales of compaction in volcanic systems. Geology 37, 471–474.

Russell, J.K., Quane, S.L., 2005. Rheology of welding: inversion of field constraints. J. Volcanol. Geotherm. Res. 142, 173–191.

Rust, A., Cashman, K.V., 2004. Permeability of vesicular silicic magma: inertial and hysteresis effects. Earth Planet. Sci. Lett. 228, 93–107.

Rust, A.C., Cashman, K.V., Wallace, P.J., 2004. Magma degassing buffered by vapor flow through brecciated conduit margins. Geology 32, 349–352.

Saar, M.O., Manga, M., 1999. Permeability–porosity relationship in vesicular basalts. Geophys. Res. Lett. 26, 111–114.

Sammis, C.G., Ashby, M.F., 1986. The failure of brittle porous solids under compressive stress states. Acta Metall. 34, 511–526. http://dx.doi.org/10.1016/0001-6160(86)90087-8.

Schipper, C.I., Castro, J.M., Tuffen, H., James, M.R., How, P., 2013. Shallow vent architecture during hybrid explosive–effusive activity at Cordón Caulle (Chile, 2011–12): evidence from direct observations and pyroclast textures. J. Volcanol. Geotherm. Res. 262, 25–37.

Shields, J.K., Mader, H.M., Pistone, M., Caricchi, L., Floess, D., Putlitz, B., 2014. Strain induced outgassing of three-phase magmas during simple shear. J. Geophys. Res. 119, 6936–6957.

Soriano, C., Giordano, D., Galindo, I., Hürlimann, M., Ardia, P., 2009. Giant gas bubbles in a rheomorphic vent fill at the Las Cañadas caldera, Tenerife (Canary Islands). Bull. Volcanol. 71, 919–932.

Sparks, R.S.J., Stasiuk, M.V., Gardeweg, M., Swanson, D.A., 1993. Welded breccias in andesite lavas. J. Geol. Soc. 150, 897–902.

Sparks, R.S.J., Tait, S.R., Yanev, Y., 1999. Dense welding caused by volatile resorption. J. Geol. Soc. 156, 217–225.

Stasiuk, M.V., Barclay, J., Carroll, M.R., Jaupart, C., Ratté, J.C., Sparks, R.S.J., Tait, S.R., 1996. Degassing during magma ascent in the Mule Creek vent (USA). Bull. Volcanol. 58, 117–130.

Stewart, M.L., 2002. Dacite block and ash avalanche hazards in mountainous terrains: 2360 yr. BP eruption of Mount Meager, British Columbia. Master of Science thesis. University of British, Columbia.

Thomas, M.E., Neuberg, J., 2012. What makes a volcano tick—a first explanation of deep multiple seismic sources in ascending magma. Geology 40, 351–354.

Tuffen, H., Dingwell, D.B., Pinkerton, H., 2003. Repeated fracture and healing of silicic magma generate flow banding and earthquakes? Geology 31, 1089–1092.

Tuffen, H., Dingwell, D.B., 2005. Fault textures in volcanic conduits: evidence for seismic trigger mechanisms during silicic eruptions. Bull. Volcanol. 67, 370–387.

Vasseur, J., Wadsworth, F.B., Lavallée, Y., Hess, K.-U., Dingwell, D.B., 2013. Volcanic sintering: timescales of viscous densification and strength recovery. Geophys. Res. Lett. 40, 5658–5664.

Wiederhorn, S.M., 1969. Fracture surface energy of glass. J. Am. Ceram. Soc. 52 (2), 99–105.

Woods, A.W., Koyaguchi, T., 1994. Transitions between explosive and effusive eruptions of silicic magmas. Nature 370, 641–644.

Wright, H.M., Cashman, K.V., 2013. Compaction and gas loss in welded pyroclastic deposits as revealed by porosity, permeability, and electrical conductivity measurements of the Shevlin Park Tuff. Geol. Soc. Am. Bull. http://dx.doi.org/10.1130/B30668.1. http://gsabulletin.gsapubs.org/content/early/2013/12/13/B30668.1.

Zhu, W., Baud, P., Wong, T.-F., 2010. Micromechanics of cataclastic pore collapse in limestone. J. Geophys. Res. 115 (B4). http://dx.doi.org/10.1029/2009JB006610.

Zhu, W., Baud, P., Vinciguerra, S., Wong, T.-F., 2011. Micromechanics of brittle faulting and cataclastic flow in Alban Hills tuff. J. Geophys. Res. 116, B06209. http://dx.doi.org/10.1029/2010JB008046.